General Analysis and Implementation of Lateral Misalignment-Adaptive WPT Systems Based on Flux-Compensation Winding

Tianhao Huang, Jingzhi Ren, and Wenxing Zhong, *Senior Member, IEEE*

***Abstract*—Based on the system architecture with one flux-compensation winding which generates compensating fluxes on the receiving winding with respect to those generated by the main transmitting winding, a general theoretical analysis is provided aiming at lateral misalignment-adaptive characteristics. In the analysis, different compensating topologies are represented with a T-type or a π-type network so that general derivations are possible. Various lateral misalignment-adaptive compensating topologies are found and summarized. With one of the possible topologies, detailed design is carried out and a 1 kW prototype is constructed for experimental verifications. The output current fluctuation of the prototype system is lower than 6% in a coupling coefficient range of 0.12–0.40 and a load resistance range of 5–20 Ω. In addition, zero-phase angle is realized in the whole coupling and load ranges.**

***Index Terms*—Inductive power transfer, misalignment adaptive, misalignment insensitive, wireless power transfer (WPT).**

I. Introduction

WIRELESS power transfer (WPT) has gradually received more and more attention in recent years, and has been applied in the wireless charging of electric vehicles, implanted medical devices, underwater robots, and consumer electronics. One of the most undesirable features of WPT systems is that the output and input of the system vary significantly as the relative position between the *TX* and the *RX* changes in a wide range. This change in the relative position is usually referred to misalignment. Even though closed-loop control methods [1], [2], [3] can be adopted for generating a constant output as required, e.g., by charging a battery. The consequences of misalignment-sensitive characteristics include high voltage-ampere (VA) rating for the primary-side inverter and resonator, large reactive power (e.g., for frequency control methods), difficulty to realize soft switching for the inverter in the whole coupling range, extra dc–dc converters needed for input voltage or output voltage regulations. Therefore, misalignment-adaptive characteristics are of great significance for WPT systems.

One way to achieve misalignment-insensitive output is to design coupler structures with moderate coupling variations in a large misalignment range [4], [5], [6]. For example, a double-D (DD) winding structure is proposed in [4]. The polarities of the currents flowing in the two windings are opposite, which produces a single-sided flux with a path height twice as large as a circular pad. The WPT system with a DD winding structure can tolerate a wider range of misalignment than that of a system with a circular winding structure [5]. In [6], a hybrid solenoid coupler whose coupling coefficient is insensitive to misalignment is studied. However, the general issue of this kind of approaches is that more windings and/or more ferrite material are usually required to generate stable coupling in a large misalignment range.

Another strategy is to optimize the parameters of the compensation topologies, making the WPT system insensitive to the position of the receiving winding [7], [8], [9], [10], [11], [12], [13], [14]. The compensation topologies include SS [7], *LCC* [8], [9], [10], *S/CLC* [11], S/SP [12], etc. Some intelligent algorithms are also applied to the optimization design process of compensating network parameters to obtain better antimisalignment characteristics and higher efficiency [13]. However, as reported in [14], most of these WPT systems with one *TX* and one *RX*, and operating with a constant frequency, share the same mathematical model despite different compensating topologies. Under the same model, the compensating parameters of all these systems could be optimized so that the system output curve is shaped into a parabolic curve as the coupling coefficient changes. This implies that a complete flat output cannot be achieved by only optimizing the compensating topologies or parameters of the WPT systems with one *TX* and one *RX*.

By combining two compensation topologies with opposite misalignment characteristics, a smooth system output over a large misalignment range may be obtained in [15] and [16]. For example, in [15], SS and *LCC-LCC* compensation topologies are combined in a parallel way, and a much better misalignment performance is achieved. In [16], a summary study is provided

Received 22 September 2024; revised 21 November 2024; accepted 5 January 2025. Date of publication 8 January 2025; date of current version 26 February 2025. Recommended for publication by Associate Editor Y. Tang. *(Corresponding author: Wenxing Zhong.)*

Tianhao Huang is with the College of Electrical Engineering, Zhejiang University, Hangzhou 310027, China (e-mail: 12010019@zju.edu.cn).

Jingzhi Ren is with the Douch Power Technology Ltd., Ningbo 315105, China (e-mail: renjingzhi@douchpower.com).

Wenxing Zhong is with the Faculty of Electrical Engineering and Computer Science, Ningbo University, Ningbo 315211, China (e-mail: zhongwenxing@nbu.edu.cn).

Color versions of one or more figures in this article are available at https://doi.org/10.1109/TPEL.2025.3527643.

Digital Object Identifier 10.1109/TPEL.2025.3527643

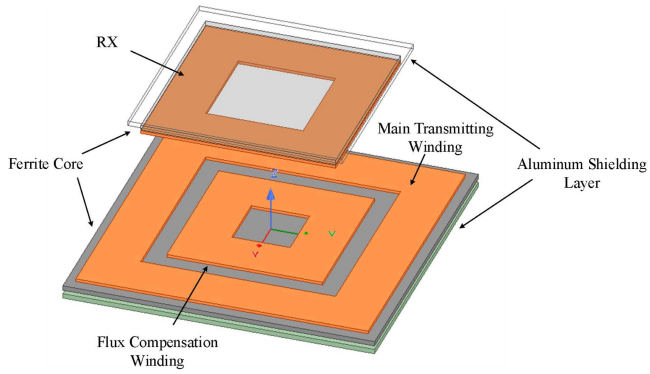

Fig. 1. Windings of a two-to-one WPT system.

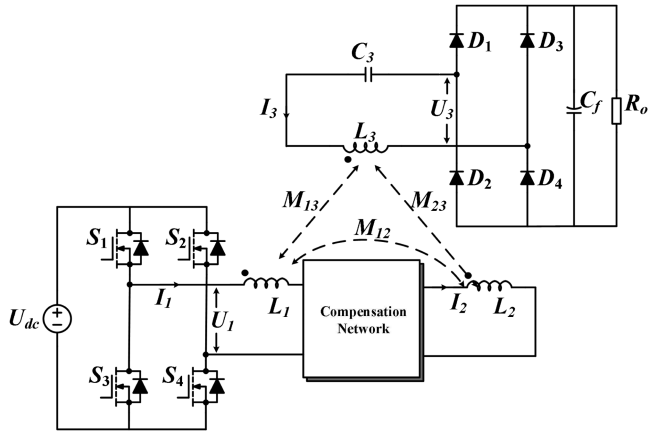

Fig. 2. Two-to-one WPT system with a general compensation network.

for different combinations of different compensation networks. These methods need to use at least two group of *TX*s and *RX*s.

In [17], antiparallel *TX* windings are used to stabilize the output power of the WPT system. The antiparallel *TX* windings are two concentric windings. The fluxes generated by the *TX* windings are with opposite directions at the *RX*, which means the induced voltages on the *RX* generated by these two *TX* windings cancel each other. When the *RX* is far away from the transmitter, i.e., with a larger lateral misalignment, the coupling between the inner *TX* winding and the *RX* is weak or even negligible due to the smaller size of the inner *TX* winding. Thereby, the canceling effect is also weak in this range. When the *RX* is close to the transmitter, the coupling between the inner *TX* winding and the *RX* is stronger and thereby, the canceling effect is more obvious. In this manner, the resultant overall coupling between the transmitter and the receiver stay relatively stable in the whole coupling range. Based on this characteristic, the inner winding is termed the flux-compensation winding in the article, because the inner winding performs a role to *compensate* some of the undesirable fluxes generated by the outer winding when the *RX* is close to the *TX*. The outer winding is the main transmitting winding. Further research on WPT with flux-compensation windings can be found in [18] and [19]. However, in [17], [18], and [19], the flux-compensation winding(s) is connected directly in series with the main transmitting winding. As a result, the lateral misalignment performance of the WPT system only relies on the design of the windings. In [20], [21], and [22], compensating component(s) are added between the main transmitting winding and the flux-compensating winding, making one more degree of design freedom for the system, and thus better lateral misalignment performances are possible.

In this article, based on the system architecture with one flux compensating winding, a general analysis is provided aiming at lateral misalignment-adaptive performance and ZPA. On the secondary side of the system, series compensation is adopted to eliminate reactive power transfer. On the primary side, the compensation circuit is considered as a two port *LC* network inserted between the main transmitting winding and the flux compensation winding to facilitate a general mathematical analysis. The two-port compensation networks are divided into two groups, i.e., T type and π-type. The conditions to enable a lateral misalignment- and load-independent output are derived. The ability to realize ZPA is also discussed. ZPA means zero reactive power attracted from the inverter, and also means both low turn-ON loss and low turn-OFF loss for the inverter switches. The general analysis provides some of the compensation topologies to realize lateral misalignment-adaptive performance for both the T type and the π-type networks. Based on the general analysis, a *CLC* π-type compensation network which can realize lateral misalignment- and load-independent output, and ZPA is taken as an example. The design method of the system with this compensation topology is introduced and a prototype system is built. Measured results of the prototype system verify the proposed design method and general model.

II. General Analysis

Fig. 1 shows the winding structure of a typical two-to-one WPT system. In the primary side, there are two windings, i.e., the main transmitting winding and the flux compensation winding coupled with each other and also coupled with the *RX*. Fig. 2 shows a general compensating method for this two-to-one WPT system. A two-port compensation network is inserted between two *TX* windings and one of the *TX* windings is connected in series to the output of the inverter. On the secondary side, the series compensation is adopted. In Fig. 2, L_1 (L_2) could be the inductance of either the main transmitting winding or the flux compensation winding. L_3 is the inductance of *RX*, and C_3 is the compensating capacitance of *RX*. *Ro* is the load resistance. The mutual inductances between every two windings are M_{12}, M_{13}, and M_{23}. The operating frequency of the full-bridge inverter is *f*. U_{in} and U_s represent the ac output voltage of the inverter and the input voltage of the rectifier, respectively. I_1, I_2, and I_3 are the currents flowing through L_1, L_2, and L_3, respectively.

Generally, the compensation network in Fig. 2 can be equivalent to two basic circuits, either T-type or π-type, as shown in Fig. 3. To simplify the analysis, a fundamental approximation method is adopted and the parasitic resistances of the compensating components are neglected.

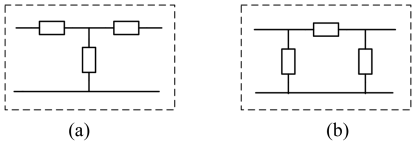

Fig. 3. Equivalent circuit of the compensation network (a) T-type. (b) π-type.

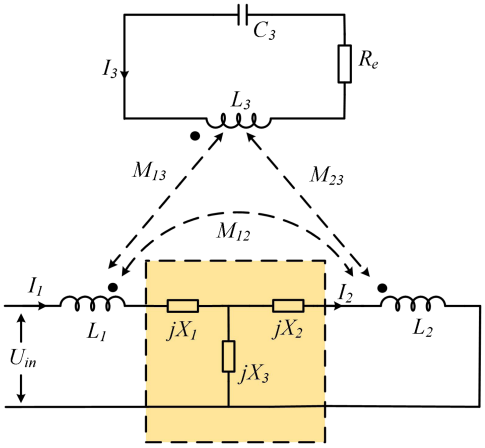

Fig. 4. System with a T-type compensation network.

A. Analysis of T-Type Compensation Network

With the T-type compensation network, the circuit topology of the system is shown in Fig. 4, where X_1, X_2, and X_3 are the reactance of the compensating elements in the T-type network. According to the Kirchhoff's laws, the circuit equation is given by

$$\begin{bmatrix} \dot{U}_{\text{in}} \\ 0 \\ 0 \end{bmatrix} = \begin{bmatrix} jX_a & -(jX_3+j\omega M_{12}) & -j\omega M_{13} \\ -(jX_3+j\omega M_{12}) & jX_b & j\omega M_{23} \\ -j\omega M_{13} & j\omega M_{23} & Z_3+R_e \end{bmatrix} \begin{bmatrix} \dot{I}_1 \\ \dot{I}_2 \\ \dot{I}_3 \end{bmatrix} \tag{1}$$

where

$$jX_a = j\omega L_1 + jX_1 + jX_3 \tag{2}$$

$$jX_b = j\omega L_2 + jX_2 + jX_3 \tag{3}$$

ω is the operating angular frequency and R_e is the equivalent load resistance. It is assumed that L_3 and C_3 are resonant at the operating frequency, i.e.,

$$Z_3 = 0. \tag{4}$$

The currents of the three windings can be derived from (1) to (4) as

$$\begin{cases} \dot{I}_1 = -\frac{\dot{U}_{\text{in}}(\omega^2 {M_{23}}^2 + jX_bR_e)}{\zeta_R + j\zeta_M} \\ \dot{I}_2 = \frac{\dot{U}_{\text{in}}[\omega^2 M_{13}M_{23} + jR_e(X_3+\omega M_{12})]}{\zeta_R + j\zeta_M} \\ \dot{I}_3 = \frac{\omega\dot{U}_{\text{in}}[X_bM_{13} - M_{23}(X_3+\omega M_{12})]}{\zeta_R + j\zeta_M} \end{cases} \tag{5}$$

where

$$\zeta_M = \omega^2\left[2M_{13}M_{23}(\omega M_{12}+X_3) - X_a{M_{23}}^2 - X_b{M_{13}}^2\right] \tag{6}$$

$$\zeta_R = R_e\left[X_aX_b - (X_3+\omega M_{12})^2\right]. \tag{7}$$

It should be noted that ξ_M is independent of the load resistance and ξ_R is independent of the coupling between each *TX* winding and *RX* winding. In the denominator expression of I_3, there is no cross term between M_{12} or M_{13} and R_e, which means the influence of the lateral misalignment and load variations can be considered separately. As a consequence, output characteristic analysis can be simplified.

A load-independent output current is normally preferred for WPT systems to achieve constant-current output without regulating the input dramatically. To achieve this characteristic, ξ_R in the expression of I_3 is set to zero, i.e.,

$$X_aX_b - (X_3+\omega M_{12})^2 = 0. \tag{8}$$

In this way, the output current is independent of the load resistance. By solving (8), four solutions can be found as follows.

1) $X_3+\omega M_{12} = \sqrt{X_aX_b}$, where both X_a and X_b are positive.
2) $X_3+\omega M_{12} = \sqrt{X_aX_b}$, where both X_a and X_b are negative.
3) $X_3+\omega M_{12} = -\sqrt{X_aX_b}$, where both X_a and X_b are positive.
4) $X_3+\omega M_{12} = -\sqrt{X_aX_b}$, where both X_a and X_b are negative.

Take solution 1) as an example. By substituting (8) into (5), the current expressions can be rewritten as

$$\begin{cases} \dot{I}_1 = \frac{\dot{U}_{\text{in}}(X_bR_e - j\omega^2{M_{23}}^2)}{\omega^2(M_{23}\sqrt{X_a} - M_{13}\sqrt{X_b})^2} \\ \dot{I}_2 = \frac{\dot{U}_{\text{in}}[\omega^2M_{13}M_{23} + jR_e(X_3+\omega M_{12})]}{j\omega^2(M_{23}\sqrt{X_a} - M_{13}\sqrt{X_b})^2} \\ \dot{I}_3 = \frac{\dot{U}_{\text{in}}}{j\omega(\chi_TM_{23} - M_{13})} \end{cases}. \tag{9}$$

The mutual inductance-related term is defined as

$$M_{\text{eq}} = \chi_TM_{23} - M_{13} \tag{10}$$

where

$$\chi_T = \sqrt{\frac{X_a}{X_b}}. \tag{11}$$

In expression (10), M_{13} and M_{23} decrease simultaneously when a lateral misalignment occurred. By properly adjusting the ratio of X_a to X_b, the effect of the lateral misalignment on the denominator can be minimized. In other words, it is possible to have a relative constant I_3 regardless of the changes in the lateral misalignment.

The input impedance Z_{in} Is Given By

$$Z_{\text{in}} = \frac{\omega^2(M_{23}\sqrt{X_a} - M_{13}\sqrt{X_b})^2}{X_b^2R_e^2 + \omega^4M_{23}^4}\left(X_bR_e + j\omega^2{M_{23}}^2\right). \tag{12}$$

Similarly, the output current I_3 and the tanθ, where θ is the input impedance angle, for all four cases can be calculated as given in Table I.

TABLE I
OUTPUT CURRENT AND PHASE ANGLE WITH DIFFERENT SOLUTIONS OF (8)

Resonance condition	X_a	X_b	I_3	$\tan\theta$
$X_3+\omega M_{12}=\sqrt{X_aX_b}$	+	+	$\frac{U_{in}}{j\omega(\chi_T M_{23}-M_{13})}$	$\frac{\omega^2 M_{23}^2}{X_bR_e}$
$X_3+\omega M_{12}=\sqrt{X_aX_b}$	-	-	$\frac{U_{in}}{j\omega(\chi_T M_{23}-M_{13})}$	$\frac{\omega^2 M_{23}^2}{X_bR_e}$
$X_3+\omega M_{12}=-\sqrt{X_aX_b}$	+	+	$\frac{U_{in}}{j\omega(\chi_T M_{23}+M_{13})}$	$\frac{\omega^2 M_{23}^2}{X_bR_e}$
$X_3+\omega M_{12}=-\sqrt{X_aX_b}$	-	-	$\frac{U_{in}}{j\omega(\chi_T M_{23}+M_{13})}$	$\frac{\omega^2 M_{23}^2}{X_bR_e}$

TABLE II
TOPOLOGIES AND OUTPUT CURRENT WITH T-TYPE COMPENSATION NETWORKS MEETING SOLUTION A)

Topology structure	Output current I_3
Topology I 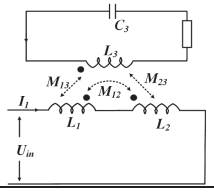	$I_3=\frac{U_{in}}{j\omega(M_{23}-M_{13})}$
Topology II 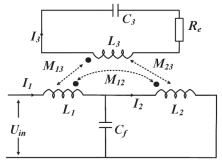	$I_3=\frac{U_{in}}{j\omega\left(\frac{L_1-M_{12}}{L_2-M_{12}}M_{23}-M_{13}\right)}$ Resonant Condition $\omega M_{12}-\frac{1}{\omega C_f}=\sqrt{(\omega L_1-\frac{1}{\omega C_f})(\omega L_2-\frac{1}{\omega C_f})}$
Topology III 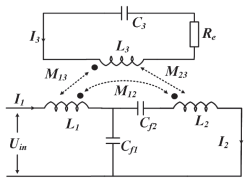	$I_3=\frac{U_{in}}{j\omega\left(\frac{L_1-M_{12}}{L_2-M_{12}}M_{23}-M_{13}\right)}$ Resonant Condition $\omega M_{12}-\frac{1}{\omega C_{f1}}=\sqrt{(\omega L_1-\frac{1}{\omega C_{f1}})(\omega L_2-\frac{1}{\omega C_{f1}}-\frac{1}{\omega C_{f2}})}$

In order to make the mutual inductance-related term M_{eq} antilateral misalignment, M_{13} and M_{23} in (10) should have the same sign. In the solution of 3) and 4), M_{13} and M_{23} in the denominator of I_3 have opposite signs.

On the other hand, the inverter output voltage should be slightly ahead of the inverter output current to ensure zero-voltage SWITCHING (ZVS). In other words, θ in (12) should be positive. Therefore, only solution 1) and 2) can achieve ZVS.

Take solution 1) as an example. Table II gives three topologies that can fulfill solution 1). Topology I is the simplest SS compensation with two series TXs. M_{eq} of this case is (M_{23}-M_{13}). To achieve lateral misalignment independent output current, (M_{23}-M_{13}) should maintain stable as the lateral misalignment changes. In other words, the decrease of M_{23} and the decrease of M_{13} as the lateral misalignment increases should be the same. However, it is difficult to design a three-winding coupler with such a characteristic. By adding a shunt capacitor (topology II) and further adding a series capacitor (topology III), more degrees of design freedom can be provided. A more stable I_3 under lateral misalignments can be achieved by adjusting the coefficients in the M_{23} term. However, as depicted in the $\dot{I}_1$ expression in (9), $\dot{I}_1$ is not in phase with $\dot{U}_{\text{in}}$ meaning ZPA cannot be realized and large reactive power may exist.

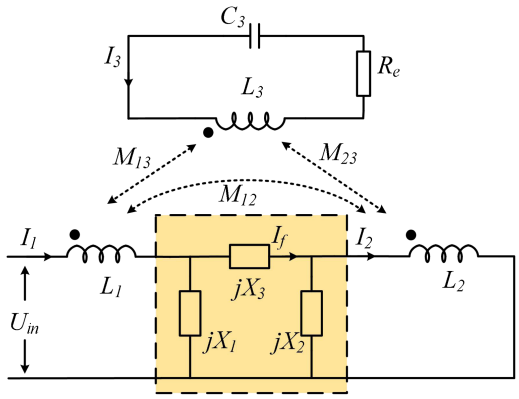

Fig. 5. System with a π-type compensation network.

B. Analysis of π-Type Compensation Network

With a π-type compensation network, the circuit topology of the system is shown in Fig. 5. According to the Kirchhoff's laws, the circuit equations are given by

$$\begin{bmatrix}\dot{U}_{\text{in}}\\0\\0\\0\end{bmatrix}=\begin{bmatrix}jX_\alpha & -jX_1 & j\omega M_{12} & j\omega M_{13}\\ -jX_1 & jX_f & -jX_2 & 0\\ j\omega M_{12} & -jX_2 & jX_\beta & j\omega M_{23}\\ j\omega M_{13} & 0 & j\omega M_{23} & Z_3+R_e\end{bmatrix}\begin{bmatrix}\dot{I}_1\\\dot{I}_f\\\dot{I}_2\\\dot{I}_3\end{bmatrix} \tag{13}$$

where

$$X_\alpha=\omega L_1+X_1 \tag{14}$$

$$X_f=X_1+X_2+X_3 \tag{15}$$

$$X_\beta=X_2+\omega L_2. \tag{16}$$

It is assumed that L_3 and C_3 are resonant at the operating frequency, i.e.,

$$Z_3=0. \tag{17}$$

The current can be derived from (13) to (17) as

$$\begin{cases}\dot{I}_1=\frac{j\dot{U}_{\text{in}}[\omega^2 M_{23}^2 X_f+jR_e(X_\beta X_f-X_2^2)]}{\sigma_M+j\sigma_R}\\ \dot{I}_f=\frac{j\dot{U}_{\text{in}}[jR_e(X_1X_\beta-\omega M_{12}X_2)-\omega^2 M_{23}(M_{23}X_1-M_{13}X_2)]}{\sigma_M+j\sigma_R}\\ \dot{I}_2=\frac{j\dot{U}_{\text{in}}[jR_e(X_1X_2-\omega M_{12}X_f)-\omega^2 M_{13}M_{23}X_f]}{\sigma_M+j\sigma_R}\\ \dot{I}_3=\frac{j\omega\dot{U}_{\text{in}}[M_{13}(X_\beta X_f-X_2^2)+M_{23}(X_1X_2-\omega M_{12}X_f)]}{\sigma_M+j\sigma_R}\end{cases} \tag{18}$$

where σ_M and σ_R are given by

$$\sigma_M = \omega^2\Big[(M_{13}X_2 - M_{23}X_1)^2 + X_f(2\omega M_{12}M_{13}M_{23} - {M_{23}}^2X_\alpha - {M_{13}}^2X_\beta)\Big] \tag{19}$$

$$\sigma_R = R_e(X_2^2X_\alpha + \omega^2{M_{12}}^2X_f + {X_1}^2X_\beta - 2\omega M_{12}X_1X_2 - X_\alpha X_f X_\beta). \tag{20}$$

The input impedance is calculated as

$$Z_{\text{in}} = \frac{\dot{U}_{\text{in}}}{\dot{I}_1} = \text{Re}[Z_{\text{in}}] + j\text{Im}[Z_{\text{in}}] \tag{21}$$

where

$$\text{Re}[Z_{\text{in}}] = \frac{\sigma_R\omega^2{M_{23}}^2X_f + \sigma_M R_e(X_\beta X_f - X_2^2)}{\left(\omega^2{M_{23}}^2X_f\right)^2 + {R_e}^2(X_\beta X_f - X_2^2)^2} \tag{22}$$

$$\text{Im}[Z_{\text{in}}] = \frac{\sigma_R R_e(X_\beta X_f - X_2^2) + \sigma_M\omega^2{M_{23}}^2X_f}{\left(\omega^2{M_{23}}^2X_f\right)^2 + {R_e}^2(X_\beta X_f - X_2^2)^2}. \tag{23}$$

To realize ZPA, Im[Z_{in}] should be zero, i.e.,

$$\sigma_R R_e(X_\beta X_f - X_2^2) + \sigma_M\omega^2{M_{23}}^2X_f = 0. \tag{24}$$

In order to realize ZPA input under any loads and coupling conditions, there should be $\sigma_R R_e(X_\beta X_f - X_2^2) = 0$ and $\sigma_M\omega^2{M_{23}}^2X_f = 0$. Two solutions can be derived as

$$\text{Solution I}: \quad \begin{cases} X_f = 0 \\ X_\beta X_f - X_2^2 = 0 \end{cases} \tag{25}$$

$$\text{Solution II}: \quad \begin{cases} X_f = 0 \\ \sigma_R = 0 \end{cases}. \tag{26}$$

By substituting (25) into (18), the current can be rewritten as

$$\begin{cases} \dot{I}_1, \dot{I}_2, \dot{I}_3 = 0 \\ \dot{I}_f = \frac{\dot{U}_{\text{in}}(-\omega^2{M_{23}}^2X_1 + jR_eX_1X_\beta)}{R_e{X_1}^2X_\beta - j\omega^2{X_1}^2{M_{23}}^2} \end{cases}. \tag{27}$$

The real power is zero in this case, therefore, Solution I is infeasible. By substituting (26) into (18), the current can be rewritten as

$$\begin{cases} \dot{I}_1 = \frac{R_e\dot{U}_{\text{in}}}{\omega^2(\chi_\pi M_{23} - M_{13})^2} \\ \dot{I}_2 = -\frac{R_e\dot{U}_{\text{in}}X_1X_2}{\omega^2(M_{23}X_1 - M_{13}X_2)^2} \\ \dot{I}_3 = \frac{j\dot{U}_{\text{in}}}{\omega(\chi_\pi M_{23} - M_{13})} \end{cases} \tag{28}$$

where χ_π is given by

$$\chi_\pi = \frac{X_1}{X_2}. \tag{29}$$

The input impendence can be expressed as

$$Z_{\text{in}} = \frac{\dot{U}_{\text{in}}}{\dot{I}_1} = \frac{\omega^2(\chi_\pi M_{23} - M_{13})^2}{R_e}. \tag{30}$$

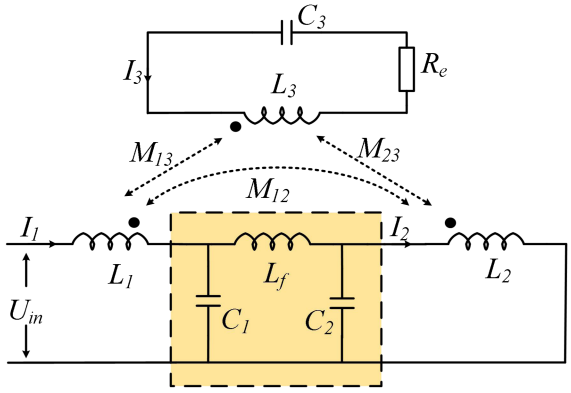

Fig. 6. *CLC* WPT system.

The mutual inductance-related term is given by

$$M_{\text{eq}} = \chi_\pi M_{23} - M_{13}. \tag{31}$$

Since the input impedance is pure resistive, ZPA is realized regardless of coupling and load conditions. As can be seen from (28), a load independent output current is obtained. To have a coupling-insensitive I_3, M_{eq} should keep constant by properly designing X_1 and X_2. Furthermore, since Z_{in} is in proportion to ${M_{\text{eq}}}^2$, a coupling-insensitive input impendence is obtained, which can ensure soft switching and a small VA rating of the inverter in the entire coupling range.

In (31), M_{13} and M_{23} could be either positive or negative. If M_{13} and M_{23} are both positive, χ_π should be positive to ensure M_{eq} in (31) to maintain stable. Consequently, X_1 and X_2 should be either both inductive or both capacitive. According to the constraints in (29), two compensation networks can be used to achieve a coupling-insensitive and load-independent CC output, which are given in Table III. In Table III, positive M_{13} and M_{23} are assumed. In these two networks, the dotted end of one of the *TX*s is connected to the undotted end of the other *TX* through the π-type compensation work. The output current and input impendence are also given in Table III.

C. *Design of* CLC π-*Type Network*

Since the T-type compensation networks given in Table II cannot realize ZPA. A *CLC* π-type network is adopted for constructing the prototype. This section will detail the process for designing a *CLC* WPT (see Fig. 6).

The currents in (28) can be rewritten as

$$\begin{cases} \dot{I}_1 = \frac{R_e\dot{U}_{\text{in}}}{\omega^2(\chi_\pi M_{23} - M_{13})^2} \\ \dot{I}_2 = -\frac{\chi_\pi R_e\dot{U}_{\text{in}}}{\omega^2(\chi_\pi M_{23} - M_{13})^2} \\ \dot{I}_3 = \frac{j\dot{U}_{\text{in}}}{\omega(\chi_\pi M_{23} - M_{13})} \end{cases}. \tag{32}$$

With (28) and (30), the compensation capacitances can be derived as

$$C_1 = -\frac{(\chi_\pi + 1)}{\omega^2(2\chi_\pi M_{12} - \chi^2 L_2 - L_1)} \tag{33}$$

$$C_2 = -\frac{\chi_\pi(\chi_\pi + 1)}{\omega^2(2\chi_\pi M_{12} - {\chi_\pi}^2 L_2 - L_1)}. \tag{34}$$

TABLE III
TOPOLOGIES, OUTPUT CURRENT, AND INPUT IMPEDANCE WITH Π-TYPE COMPENSATION NETWORKS WITH POSITIVE M_{13} AND M_{23}

Compensation Network	Topology Scheme	Output Current I_3	Input Impendence Z_{in}
CLC (For the prototype)	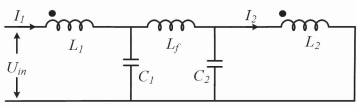	$\frac{jU_{in}}{\omega(\frac{C_2}{C_1}M_{23}-M_{13})}$	$\frac{\omega^2(\frac{C_2}{C_1}M_{23}-M_{13})^2}{R_e}$
LCL	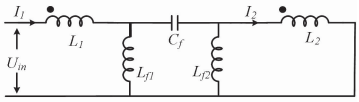	$\frac{jU_{in}}{\omega(\frac{L_{f1}}{L_{f2}}M_{23}-M_{13})}$	$\frac{\omega^2(\frac{L_{f1}}{L_{f2}}M_{23}-M_{13})^2}{R_e}$
CLL	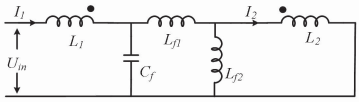	$\frac{jU_{in}}{\omega(M_{13}-\frac{1}{\omega^2C_fL_{f2}}M_{23})}$	$\frac{\omega^2(M_{13}-\frac{1}{\omega^2C_fL_{f2}}M_{23})^2}{R_e}$
LLC	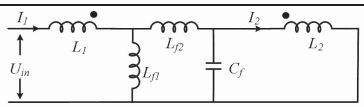	$\frac{jU_{in}}{\omega(M_{13}-\omega^2C_fL_{f1}M_{23})}$	$\frac{\omega^2(M_{13}-\omega^2C_fL_{f1}M_{23})^2}{R_e}$
CCL	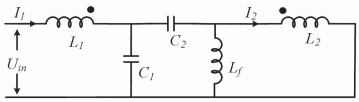	$\frac{jU_{in}}{\omega(M_{13}-\frac{1}{\omega^2C_1L_f}M_{23})}$	$\frac{\omega^2(M_{13}-\frac{1}{\omega^2C_1L_f}M_{23})^2}{R_e}$
LCC	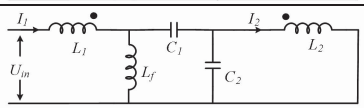	$\frac{jU_{in}}{\omega(M_{13}-\omega^2C_2L_fM_{23})}$	$\frac{\omega^2(M_{13}-\omega^2C_2L_fM_{23})^2}{R_e}$

TABLE IV
GIVEN PARAMETERS

Parameter	Description	Value
U_d	Input dc source voltage	90 V
P_o	Output Power	1 kW
R_o	Load resistance	20 Ω
h	Air gap	100 mm
f	Operating frequency	85.5 kHz
D_{po}	*TX*1 outer length	400 mm
D_{so}	*RX* outer length	400 mm
D_{si}	*RX* inner length	100 mm

The compensation inductor L_f can be calculated

$$L_f = -\frac{X_1 + X_2}{\omega}. \tag{35}$$

D. Design of Coupler Parameters

The given parameters of the system are given in Table IV.

The expected mutual inductance-related term can be rewritten as

$$M_{\mathrm{eq0}} = \frac{64}{\pi^4}\frac{U_d\sqrt{R_o}}{\omega\sqrt{P_o}}. \tag{36}$$

Altering the number of turns N_s or the dimensions of *RX* will impact both M_{13} and M_{23} concurrently. Therefore, the parameters of *RX* are determined first. Generally, lower number of turns will be adopted with a larger winding current to ensure a high efficiency. In this article, efficiency optimization is not the focus, so N_s is empirically chosen as 30. But it should be noted that N_s can be further optimized for a higher power transfer efficiency.

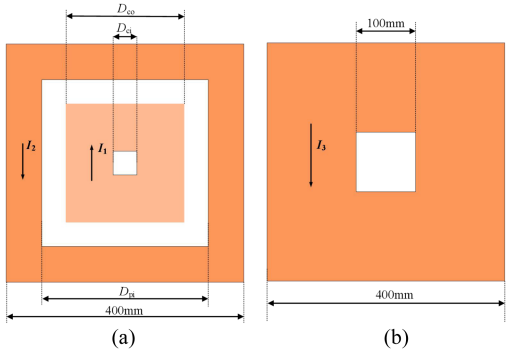

Fig. 7. Designed winding structures of (a) primary side. (b) Secondary side.

With (32)–(36), the currents that flow through the windings can be calculated and the specifications of the wires can be determined.

Fig. 7 illustrates the winding parameters of *TX* and *RX*. The parameters to be optimized are the inner diameter D_{pi} and the number of turns N_p for *TX*1, the outer diameter D_{co}, the inner diameter D_{ci}, and the number of turns N_c for *TX*2. In the rest of this article, the lateral misalignment is normalized to the outer length of the pads, i.e., 400 mm.

Finite element analysis (FEA) simulations are run to obtain the inductances. The optimization process aims to determine the optimal value of χ_π that produces the most stable mutual inductance-related term. Fig. 8 shows the changes in the equivalent mutual inductance-related term with the variation of lateral misalignment distance with different χ_π. The most stable M_{eq} corresponding χ_π can be identified.

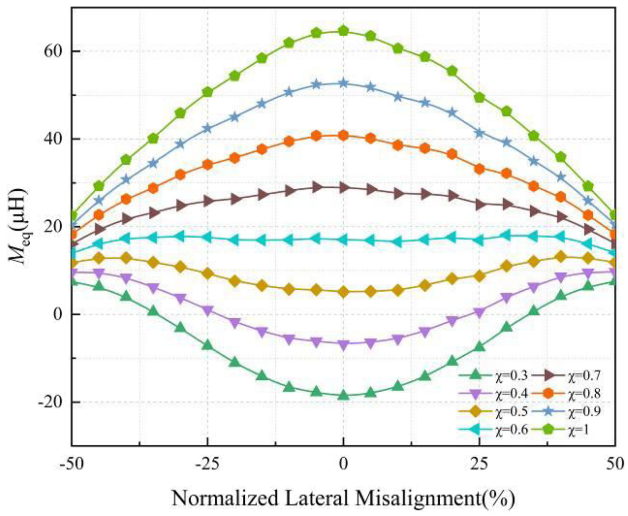

Fig. 8. Mutual inductance-related term versus lateral misalignment of the designed winding structure.

TABLE V
DESIGNED WINDING PARAMETERS

	N_p	N_c	D_{pi}	D_{co}	D_{ci}
CASE I	15	15	280 mm	220 mm	100 mm
CASE II	10	10	320 mm	280 mm	200 mm
CASE III	15	20	280 mm	200 mm	40 mm

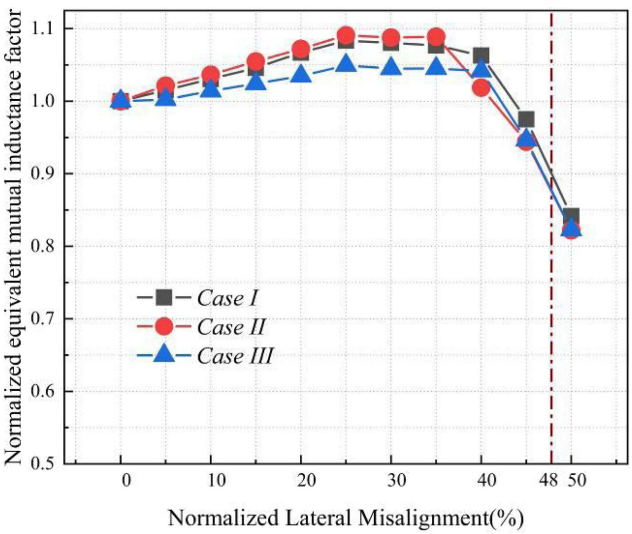

Fig. 9. Mutual inductance-related term versus lateral x-misalignment of three designed winding structures.

By scanning the parameters of the windings, optimal designs which have stable M_{eq} close to M_{eq0} in the interested lateral misalignment range can be found. For example, three possible designs for the prototype are given in Table V. Fig. 9 shows M_{eq} of these three designs within the lateral misalignment range. Case III has the most stable M_{eq} compared with the other two cases. In the range of 0–190 mm lateral misalignment, which corresponding to the 48% of the maximum size of the primary

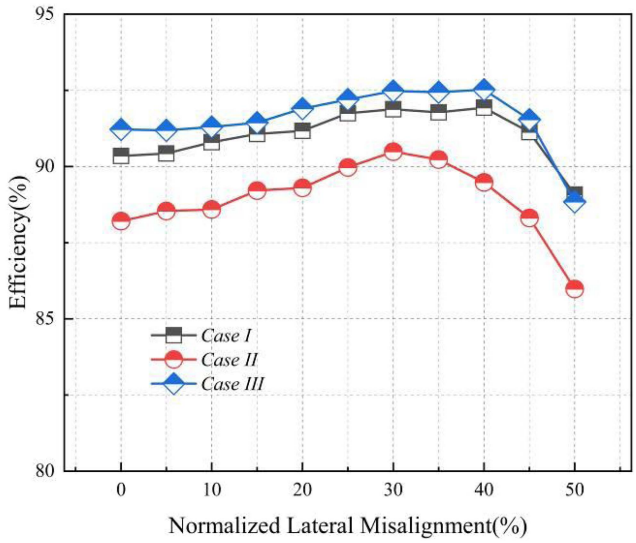

Fig. 10. AC–AC efficiency of the system with the three designed winding structures.

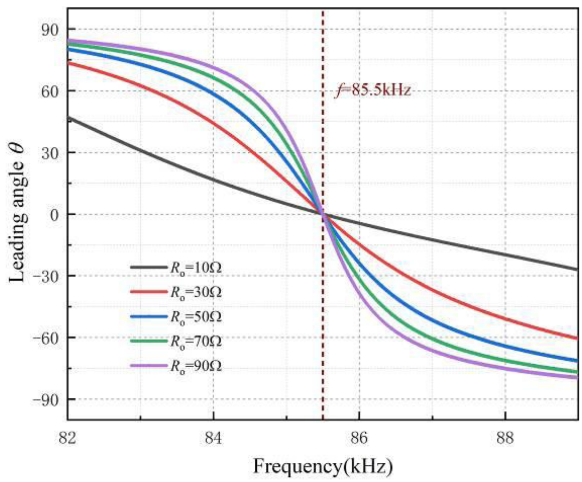

Fig. 11. Calculated θ at the aligned position of the prototype system.

coils, the mutual inductance-related term changes less than the predetermined value.

To compare the efficiencies of three designs, the quality factors of the compensating inductors and capacitors are assumed to be 500 and 1000, respectively. By substituting (41)–(44) into the circuit model, the ac–ac efficiencies of the systems with the three different *TX* winding structures can be calculated, as given Fig. 10. It is clear that case III has the highest efficiency curve among these three. Therefore, case III is selected for constructing the prototype.

E. Theoretical Characteristics of Prototype System

The calculated phase angles (θ) that the input voltage leading the input current at the aligned position are shown in Fig. 11, with different load resistances and different operating frequencies. At the desired frequency point, i.e., 85.5 kHz, the input voltage

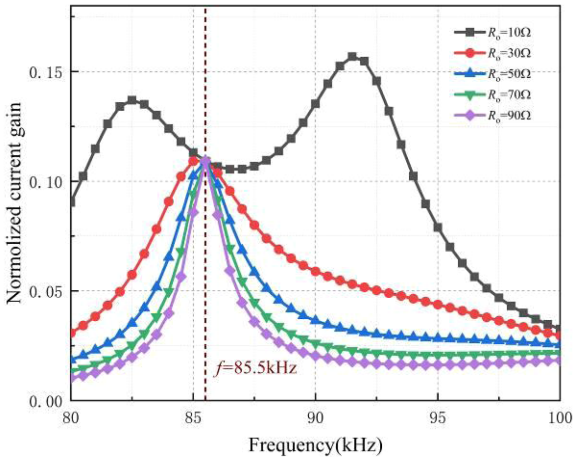

Fig. 12. Calculated current gain I_o/U_{in} at the aligned position of the prototype system.

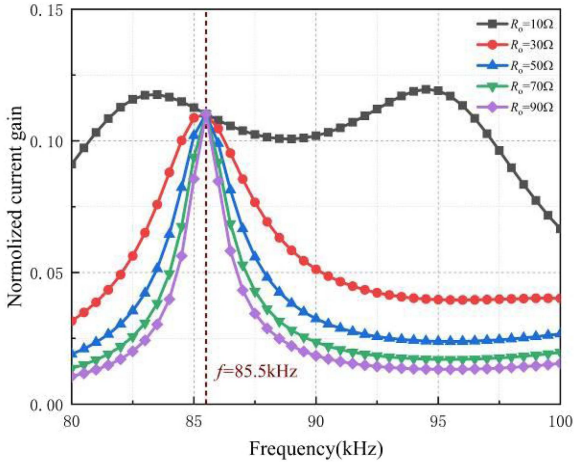

Fig. 14. Calculated current gain I_o/U_{in} at the misaligned position (100 mm) of the prototype system.

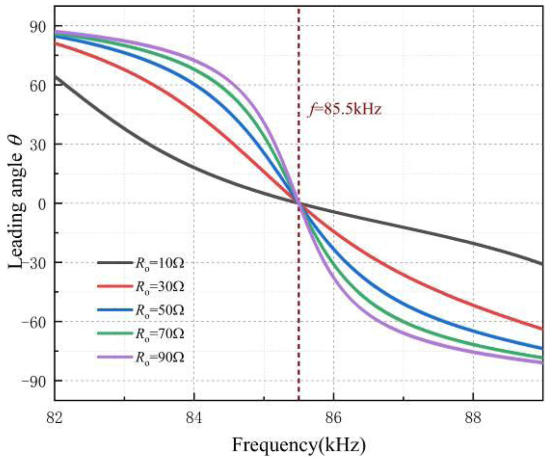

Fig. 13. Calculated θ at the misaligned position (100 mm) of the prototype system.

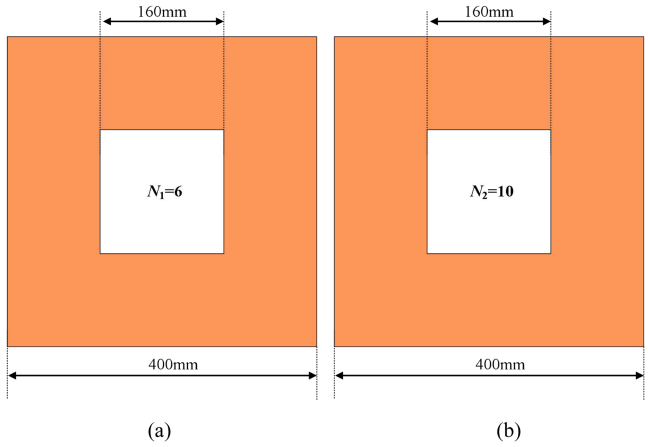

Fig. 15. Designed windings of the SS system (a) primary side. (b) Secondary side.

and the input current are always in phase regardless of the load resistance. This proves that the ZPA characteristic of the prototype system is not affected by the load

The curve of the current transfer ratio I_o/U_{in} with different operating frequencies at the aligned position is shown Fig. 12 at 85.5 kHz, the current transfer ratio is independent of the load resistance. Thereby, CC output is achieved at this operating frequency.

Similarly, Fig. 13 shows the θ-f curve at the position with a lateral misalignment distance of 100 mm, which corresponding to the 25% of the maximum size of the primary coils. Fig. 14 indicates that ZPA is realized at 85.5 kHz regardless of the load resistance. Figs. 11 and 13 verify that the ZPA characteristic of the proposed system is not affected by the load condition and the lateral misalignment condition. In other words, zero reactive power is needed within the load range and also the lateral misalignment range.

Fig. 14 shows the I_o/U_{in}-f curve at the position with a lateral misalignment distance of 100 mm. Again, CC output is realized at 85.5 kHz. Moreover, the current gain at 85.5 kHz is close to the one at the aligned position as shown in Fig. 12. Therefore, Figs. 12 and 14 verifie that a stable output current can be achieve by the proposed system under load changes and also coupling changes.

In short, the proposed *CLC* three-winding WPT system can maintain ZPA and CC with different load resistances and different lateral misalignment positions.

In addition, the performance of the proposed *CLC* three-winding WPT system is compared with that of a conventional SS two-winding WPT system. The SS two-winding system has the load-independent CC output characteristic which is the same as the proposed system. For a fair comparison, the conventional two-winding system and the proposed three-winding system should have the same pad size for both the transmitter and the receiver. Under this assumption, the SS system is designed according to the method introduced in [23]. The designed windings of the SS system are shown in Fig. 15 and the key parameters are given in Table VI. The designed SS system generates the same output power as the proposed system without input voltage regulation at the aligned position. Fig. 16 shows the theoretical

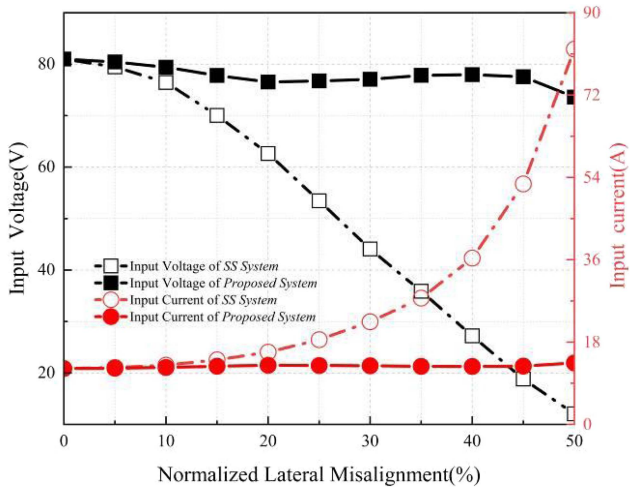

Fig. 16. Input voltage and current versus lateral misalignment.

TABLE VI
PARAMETERS OF SS WPT SYSTEM

Parameter	Description	Value
L_1	Inductance of winding TX	20.245 μH
L_2	Inductance of winding RX	53.93 μH
C_1	Compensation capacitor of TX	172.6 nF
C_2	Compensation capacitor of RX	64.19 nF
M_{12}	Mutual inductance of TX and RX	13.54 μH

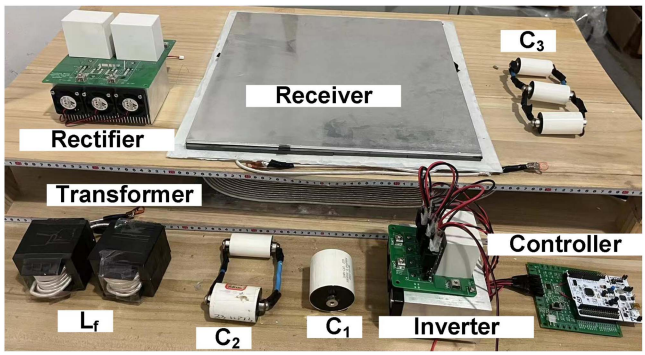

Fig. 17. Experimental prototype.

input voltages and currents of these two systems for maintaining the same required output power. For the conventional system, the input current needs to rapidly increase while the input voltage simultaneously decreases to maintain the same output power. The consequence is the significantly increasing losses in the inverter and the primary resonator. In contrast, the input voltage and current of the proposed system are stable in the lateral misalignment range.

III. EXPERIMENTAL VERIFICATION

A 1 kW prototype is built for experiment, as shown in Fig. 17. The MOSFETs of the inverter is C3M0021120D from CREE and the diodes of the rectifier is MUR3060PT from YANGJIE. The

TABLE VII
COMPENSATION PARAMETERS OF PROPOSED *CLC-S* WPT SYSTEM

Parameter	Description	Value
L_1	Inductance of winding $TX1$	95.60 μH
L_2	Inductance of winding $TX2$	233.9 μH
L_3	Inductance of winding RX	419.3 μH
L_f	Inductance of compensation inductor	220.2 μH
C_1	Compensation capacitor of $TX1$	40.55 nF
C_2	Compensation capacitor of $TX2$	26.32 nF
C_3	Compensation capacitor of RX	8.210 nF
M_{12}	Mutual inductance of $TX1$ and $TX2$	40.98 μH
M_{13}	Mutual inductance of $TX1$ and RX	62.48 μH
M_{23}	Mutual inductance of $TX2$ and RX	125.1 μH

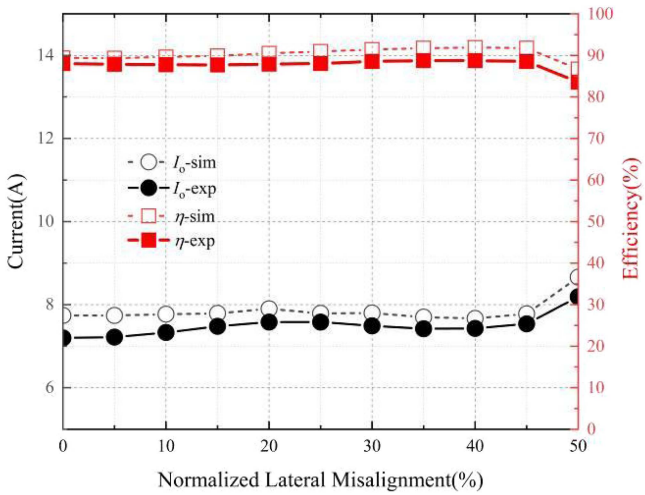

Fig. 18. Simulation and experimental results of the output current $I3$ and the DC–DC efficiency of the prototype system in the lateral misalignment range.

inverter is supplied by a dc power source IT6522D from ITECH. The operating frequency is 85.5 kHz. The control signal is given by the STM32F334 controller. Litz wire of 0.1 mm strand diameter and 800 strands is used. The ferrite cores are made of DMR95 material with a thickness of 5 mm. Both the transmitting coil and the receiving coil are shielded by aluminum plates to reduce the magnetic leakage of the system. The compensation parameters are given in Table VII.

Table VIII given the waveforms of the input voltage (i.e., inverter output voltage), the input current, U_3 and I_3 at load resistances of $Ro = 5\ \Omega$, $10\ \Omega$, and $20\ \Omega$ and at different RX positions. The output current of the system varies in the range of 7.97–9.02 A, under the test conditions of well aligned, 25% normalized lateral misalignment and 45% normalized lateral misalignment, when the load resistance changes by four times, the output current changes by 4.3%, 5.5%, and 5.0% respectively, which can prove the proposed system has good load-independent output capability. Meanwhile, as can be seen from the input voltage and the input current waveforms, ZPA is perfectly realized in all the load and coupling conditions.

The measured output current and efficiency are compared with the simulation values in Fig. 18 with a load resistance of 20 Ω. It can be seen that within the 0–180 mm lateral misalignment range (coupling coefficient range of 0.40–0.12), the output current of rectifier varies in the range of 7.2 to 7.58 A, i.e, the variation

TABLE VIII
WAVEFORMS OF INPUT AND OUTPUT VOLTAGE AND CURRENT

Misalignment	5 Ω Waveforms	10 Ω Waveforms	20 Ω Waveforms
Aligned	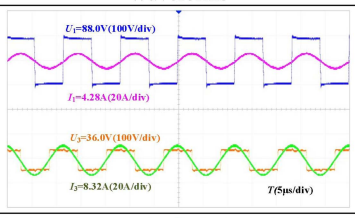	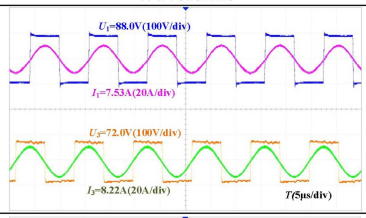	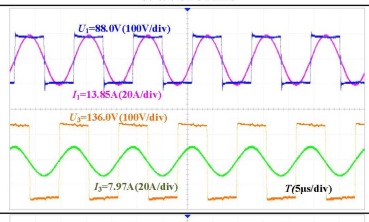
25% Normalized Misalignment	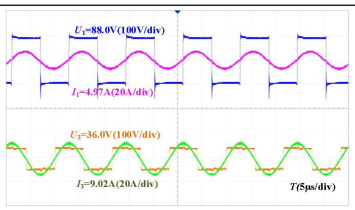	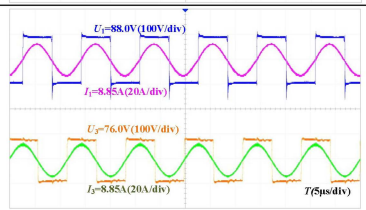	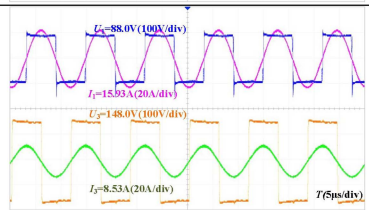
45% Normalized Misalignment	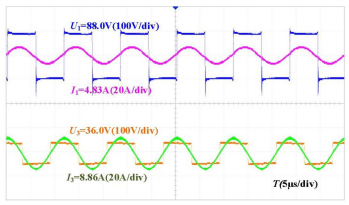	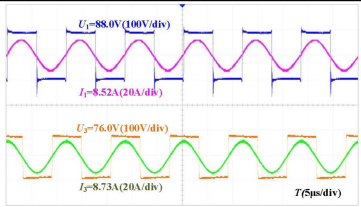	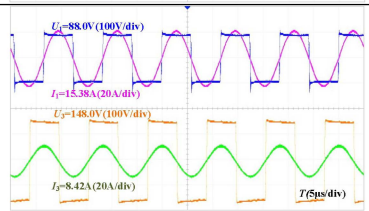

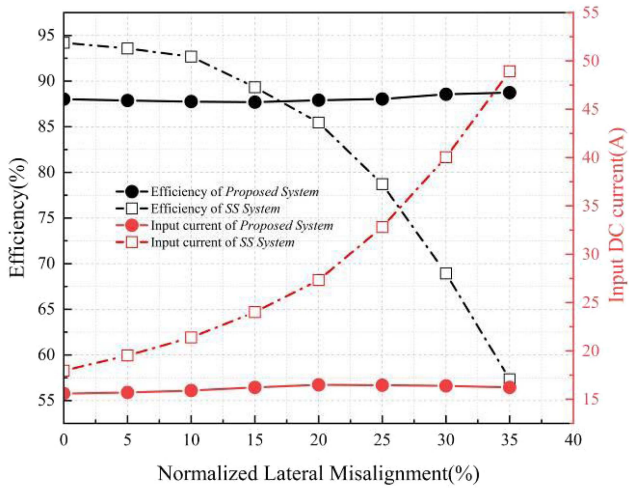

Fig. 19. Measured dc–dc efficiencies and input current I_1 of the prototype system and the SS system.

of output current is no more than 5.1%. The maximum output current is located at the lateral misalignment distance of 100 mm, which is consistent with the simulation results. The measured dc–dc efficiency at the aligned position is 88.0% with an output power of 1.08 kW. In the range of 0%–45% normalized lateral misalignment the prototype system maintains a stable efficiency.

A comparison is done between the aforementioned SS system and the proposed system. The measured parameters of the SS system are given in Table VI. The input currents and the dc–dc efficiencies of the proposed system and the SS system are recorded in Fig. 19 as the lateral misalignment changes in the range of 0–140 mm, which corresponding to the 35% of the maximum size of the primary coils. At the aligned position with zero misalignment, the efficiency of the proposed system is lower since the flux cancellation strategy is adopted. However, as the lateral misalignment increases, the efficiency of the conventional SS system decreases rapidly as predicted by the previous analysis. At the position with 140 mm lateral misalignment, the input current of the SS system has increased to about three times the value at the aligned position and the efficiency drops to 57%. In contrast, the efficiency of the proposed system stays at about 88% over the misalignment range.

IV. CONCLUSION

General compensation topologies are theoretically studied, aiming at finding a solution for generating a lateral misalignment- and load- independent output. These compensation topologies are divided into two groups, i.e., T type and π-***type***. The T-***type*** compensation topologies can theoretically achieve load-independent output with high lateral misalignment tolerance, but cannot realize ZPA. While the π-*type* compensation topologies can realize lateral misalignment- and load-independent output, and meanwhile maintain ZPA. Based on one of the π-*type* compensation topologies

In this article, a *two-port* compensation network is inserted between the two *TX* windings of a three-winding WPT system. Through mathematical analysis, it is found that if the *two-port* compensation network is a T-*type LC* network, lateral misalignment- and load-independent output may be achieved, but ZPA cannot be guaranteed; if it is a π-*type LC* network, all three objectives (lateral misalignment-independent, load-independent output, and ZPA) can be realized. As an example,

a *CLC* π-type *LC* network is investigated in detailed. A prototype system based on this compensation method is constructed and experimental results show that the output current of the prototype system remains stable in the given lateral misalignment and load ranges. ZPA is also perfectly maintained over the whole operation ranges. In comparison to the conventional two-coil system, the newly proposed method exhibits decreased efficiency under alignment conditions and entails higher costs and larger dimensions. Nevertheless, this approach leads to a reduction in both output power and system efficiency, as well as a decrease in input current stress. These outcomes highlight promising prospects for practical application and underscore the research significance of this method.

REFERENCES

[1] M. J. Neath, A. K. Swain, U. K. Madawala, and D. J. Thrimawithana, "An optimal PID controller for a bidirectional inductive power transfer system using multiobjective genetic algorithm," *IEEE Trans. Power Electron.*, vol. 29, no. 3, pp. 1523–1531, Mar. 2014.

[2] W. X. Zhong and S. Y. R. Hui, "Maximum energy efficiency tracking for wireless power transfer systems," *IEEE Trans. Power Electron.*, vol. 30, no. 7, pp. 4025–4034, Jul. 2015.

[3] E. Gati, G. Kampitsis, and S. Manias, "Variable frequency controller for inductive power transfer in dynamic conditions," *IEEE Trans. Power Electron.*, vol. 32, no. 2, pp. 1684–1696, Feb. 2017.

[4] M. Budhia, J. T. Boys, G. A. Covic, and C.-Y. Huang, "Development of a single-sided flux magnetic coupler for electric vehicle IPT charging systems," *IEEE Trans. Ind. Electron.*, vol. 60, no. 1, pp. 318–328, Jan. 2013.

[5] R. Bosshard, U. Iruretagoyena, and J. W. Kolar, "Comprehensive evaluation of rectangular and double-D coil geometry for 50 kW/85 kHz IPT system," *IEEE J. Emerg. Sel. Top. Power Electron.*, vol. 4, no. 4, pp. 1406–1415, Dec. 2016.

[6] A. Tejeda, S. Kim, F. Y. Lin, G. A. Covic, and J. T. Boys, "A hybrid solenoid coupler for wireless charging applications," *IEEE Trans. Power Electron.*, vol. 34, no. 6, pp. 5632–5645, Jun. 2019.

[7] H. Feng, T. Cai, S. Duan, X. Zhang, H. Hu, and J. Niu, "A dual-side-detuned series–series compensated resonant converter for wide charging region in a wireless power transfer system," *IEEE Trans. Ind. Electron.*, vol. 65, no. 3, pp. 2177–2188, Mar. 2018.

[8] H. Feng, T. Cai, S. Duan, J. Zhao, X. Zhang, and C. Chen, "An LCC-compensated resonant converter optimized for robust reaction to large coupling variation in dynamic wireless power transfer," *IEEE Trans. Ind. Electron.*, vol. 63, no. 10, pp. 6591–6601, Oct. 2016.

[9] Q. Zhu, L. Wang, Y. Guo, C. Liao, and F. Li, "Applying LCC compensation network to dynamic wireless EV charging system," *IEEE Trans. Ind. Electron.*, vol. 63, no. 10, pp. 6557–6567, Oct. 2016.

[10] J. Li, X. Zhang, and X. Tong, "Research and design of misalignment-tolerant LCC–LCC compensated IPT system with constant-current and constant-voltage output," *IEEE Trans. Power Electron.*, vol. 38, no. 1, pp. 1301–1313, Jan. 2023.

[11] Y. Yao, Y. Wang, X. Liu, Y. Pei, D. Xu, and X. Liu, "Particle swarm optimization-based parameter design method for S/CLC-compensated IPT systems featuring high tolerance to misalignment and load variation," *IEEE Trans. Power Electron.*, vol. 34, no. 6, pp. 5268–5282, Jun. 2019.

[12] Y. Wang, J. Mai, Y. Yao, and D. Xu, "Analysis and design of an IPT system based on S/SP compensation with improved output voltage regulation," *IEEE Trans. Ind. Inform.*, vol. 16, no. 5, pp. 3256–3266, May 2020.

[13] Q. Wang et al., "Inductive power transfer system with constant current-constant voltage charging tolerating misalignment based on multi-objective optimization for compensation topology," *IEEE Trans. Power Electron.*, vol. 40, no. 3, pp. 4581–4591, Mar. 2025.

[14] Y. Yao and W. Zhong, "General model and analysis of misalignment characteristics of fixed-frequency WPT systems," *IEEE Trans. Power Electron.*, vol. 38, no. 11, pp. 13315–13328, Nov. 2023.

[15] L. Zhao, D. J. Thrimawithana, and U. K. Madawala, "Hybrid bidirectional wireless EV charging system tolerant to pad misalignment," *IEEE Trans. Ind. Electron.*, vol. 64, no. 9, pp. 7079–7086, Sep. 2017.

[16] X. Qu, Y. Yao, D. Wang, S.-C. Wong, and C. K. Tse, "A family of hybrid IPT topologies with near load-independent output and high tolerance to pad misalignment," *IEEE Trans. Power Electron.*, vol. 35, no. 7, pp. 6867–6877, Jul. 2020.

[17] W.-S. Lee, W.-I. Son, K.-S. Oh, and J.-W. Yu, "Contactless energy transfer systems using antiparallel resonant loops," *IEEE Trans. Ind. Electron.*, vol. 60, no. 1, pp. 350–359, Jan. 2013.

[18] Y. Zhuang, A. Chen, C. Xu, Y. Huang, H. Zhao, and J. Zhou, "Range-adaptive wireless power transfer based on differential coupling using multiple bidirectional coils," *IEEE Trans. Ind. Electron.*, vol. 67, no. 9, pp. 7519–7528, Sep. 2020.

[19] C. Zhang, Y. Yao, and Y. Wang, "Decoupling optimization of the three-coil coupler for IPT system featuring high efficiency and misalignment to1lerance," *IEEE Trans. Ind. Electron.*, vol. 70, no. 9, pp. 8918–8927, Sep. 2023.

[20] Z. Yan et al., "Fault-tolerant wireless power transfer system with a dual-coupled LCC-S topology," *IEEE Trans. Veh. Technol.*, vol. 68, no. 12, pp. 11838–11846, Dec. 2019.

[21] Z. Yuan, M. Saeedifard, C. Cai, Q. Yang, P. Zhang, and H. Lin, "A misalignment tolerant design for a dual-coupled *LCC* -S-compensated WPT system with load-independent CC output," *IEEE Trans. Power Electron.*, vol. 37, no. 6, pp. 7480–7492, Jun. 2022.

[22] T. Li et al., "Analysis and design of rotary wireless power transfer system with dual-coupled XLC/S compensation topology," *IEEE Trans. Ind. Appl.*, vol. 59, no. 2, pp. 2639–2649, Mar./Apr. 2023.

[23] R. Bosshard, "Multi-objective optimization of inductive power transfer systems for EV charging," 2015.

Tianhao Huang was born in Hebei Province, China, in 1998. He received the B.Eng. degree in electrical engineering and its automation from the Harbin Institute of Technology, Harbin, China, in 2020. He is currently working toward the Ph.D. degree in electrical engineering with the College of Electrical Engineering, Zhejiang University, Hangzhou, China.

His current research interests include wireless power transfer technologies and power electronics.

Jingzhi Ren received the B.Eng. degree in electrical engineering from the Shandong University, Jinan, China, in 2019, and the M.S. degree in electrical engineering from the Zhejiang University, Hangzhou, China, in 2022.

He is currently a Senior Engineer with Ningbo Douch Power Technology Company Ltd., Ningbo, China. His current research interests include wireless power transfer technologies and power electronics.

Wenxing Zhong (Senior Member, IEEE) received the B.Eng. degree in electrical engineering from Tsinghua University, Beijing, China, in 2007, and the Ph.D. degree in electrical engineering from the City University of Hong Kong, Hong Kong, in 2012.

He is currently a Professor with the Faculty of Electrical Engineering and Computer Science, Ningbo University, Zhejiang, China. From 2016 to 2017, he was a Research Assistant Professor with the Department of Electrical and Electronic Engineering, the University of Hong Kong, Hong Kong. From 2017 to 2024, he was a Professor with Zhejiang University, Zhejiang, China. His research interests include wireless power transfer and power electronics.

Dr. Zhong was the recipient of the Transactions on Power Electronics First Prize Paper Award in 2015 and 2016, respectively.